



Article

Large-Scale Land Deformation Monitoring over Southern California with Multi-Path SAR Data

Meng Ao ¹, Xiaotian Wang ¹, Ying Sun ¹, Fang Wang ¹, Huanan Zhang ², Lianhuan Wei ^{1,*}, Shanjun Liu ¹ and Dong Yang ³

¹ College of Resources and Civil Engineering, Northeastern University, Shenyang 110004, China

² Liaoning Geological and Mineral Survey Institute Co., Ltd., Shenyang 110032, China

³ Liaoning Natural Resources Affairs Service Center, Shenyang 110032, China

* Correspondence: weilianhuan@mail.neu.edu.cn

Abstract: Southern California, USA, has been suffering severe surface deformation due to its active crustal movement under the north–south compression of the Pacific Plate and North American Plate. Meanwhile, affected by groundwater extraction and recharge, oil exploitation, surface subsidence, uplift, and seasonal deformation occur commonly in this region. In this paper, multi-path SAR datasets were collected to investigate and monitor surface deformation in Southern California. The unified simultaneous least squares (USLS) approach is applied to remove the deformation discontinuity between adjacent SAR image paths. Multiple deformation patterns of structural faults, groundwater withdrawal, and oil exploitation are observed with the interferometric synthetic aperture radar (InSAR) technique. The InSAR-derived results were validated with GPS monitoring data. The correlations between land deformation and groundwater withdrawal, faults, and precipitation were intensively analyzed, finding out and mastering the magnitude and characteristics of ground deformation in Southern California.

Keywords: Southern California; InSAR; groundwater withdrawal; structural faults; oil exploitation



Citation: Ao, M.; Wang, X.; Sun, Y.; Wang, F.; Zhang, H.; Wei, L.; Liu, S.; Yang, D. Large-Scale Land Deformation Monitoring over Southern California with Multi-Path SAR Data. *Remote Sens.* **2023**, *15*, 143. <https://doi.org/10.3390/rs15010143>

Academic Editors: Antonio Pepe, Jiayi Pan, Fusun Balik Sanli and Qing Zhao

Received: 23 November 2022

Revised: 19 December 2022

Accepted: 20 December 2022

Published: 27 December 2022



Copyright: © 2022 by the authors. Licensee MDPI, Basel, Switzerland. This article is an open access article distributed under the terms and conditions of the Creative Commons Attribution (CC BY) license (<https://creativecommons.org/licenses/by/4.0/>).

1. Introduction

Ground deformation is a global problem, and almost 45 states in the United States have been affected by it. The traditional measuring tools, such as GPS and leveling, have high monitoring accuracy, but the spatial density of the observation network is low and needs lots of fieldwork, with great labor intensity, a long operation period, and a high cost. The coverage of non-contact monitoring technologies such as unmanned aerial vehicle remote sensing (UAVRS), light detection and ranging (LiDAR), and ground-based synthetic aperture radar (GB-SAR) is greatly limited to investigate and monitor large-scale ground deformation. Optical remote sensing is greatly affected by weather conditions and cannot observe the small deformation signal. With the improvement of SAR data type and quality, the application of InSAR technology has been gradually expanded and deepened and has been successfully applied in the monitoring geological disasters such as earthquake coseism and aftershock, volcanic expansion and contraction, landslide disaster, land subsidence caused by natural factors [1–5], and coal mine collapse, instability of high and steep slope in drainage area, bridge, highway construction, buildings, and structures monitoring caused by anthropogenic factors [6–12]. Since the 21st century, InSAR has been widely used in surface deformation monitoring due to its characteristics of high monitoring precision, high spatial resolution, high temporal repetition observation, wide coverage, and a small impact of climate conditions. However, when it comes to a larger range of surface deformation monitoring, it is necessary to solve the problem of connecting multi-path SAR results. The spatial coordinate system and the reference datum of deformation results from different SAR data with multi-path should be unified.

This study area is Southern California, USA, where crustal movement is active and surface subsidence, uplift, and seasonal deformation occur frequently [13]. Researchers have applied InSAR technology to surface deformation in this area. Gabriel (1989) first monitored the swelling and shrinkage of clay in the farmland of California's Imperial Valley [14]. Massonnet (1997) obtained the deformation field caused by geothermal exploitation in California [15]. Ferretti (2000) applied Permanent Scatterers Interferometry technology (PS-InSAR) to investigate the Pomona–Ontario basin deformation [16]. Bawden (2001) found seasonal deformation of the Santa Ana basin [17]. Zhang (2012) proposed the Temporary Coherent Point InSAR technology (TCP-InSAR) to estimate the long-term deformation rate without the need for phase unwrapping with 32 ERS-1/2 images from October 1995 to December 2000, and the results are in good agreement with the GPS observations [18]. Hu (2013) presented a weighted least squares method to obtain surface deformation in Los Angeles from 2003 to 2007 with 18 ENVISAT ASAR images [19]. Ao (2020) modified the Small Baseline Subset technology (SBAS) deformation inversion model by incorporating horizontal deformation parameters in east–west and north–south directions to improve the continuity of time series deformation monitoring and characterize the three-dimensional (3-D) deformation field of this study area accurately with the variance component estimation (VCE) method [20].

In this research, multi-path SAR datasets were collected to investigate and monitor surface deformation in Southern California. The USLS approach is applied to solve the problem of the deformation discontinuity between adjacent SAR images paths, and a hysteresis effect of 3 to 4 months was found between InSAR deformation and precipitation by the cross wavelet transform. Multiple deformation patterns were characterized through the analysis of the deformation rate and time series combined with GPS measurements.

2. Research Area and Datasets

2.1. Research Area Overview

Southern California is one of the most active tectonic regions in the world, under the north–south compression of the Pacific Plate and the North American Plate. Earthquakes occur frequently [17,21–24]. In addition, the geological structure is complex, and many faults are distributed, such as the Newport–Inglewood Fault, the San Andreas Fault, the Chino Fault, and the Raymond Fault [25]. The climate type in much of southern California is described as a Mediterranean climate, with winter rains and dry, hot summers. This area is densely populated and has frequent groundwater resource harvesting activities. For example, the Pomona–Ontario Basin and the San Bernardino Basin are typical groundwater over-withdrawal areas [16,26]. Meanwhile, there are abundant mineral resources and many oilfields, such as Inglewood Oilfield, Santa Fe Springs Oilfield, and Wilmington Oilfield [27]. Due to groundwater extraction and recharge and oil exploitation, which are affected by faults, surface subsidence, uplift, and seasonal periodic deformation occur in many areas.

2.2. Datasets

Three C-band ENVISAT ASAR datasets (tracks 442, 170, and 120) were collected in this study. There are 33 ascending images from November 2005 to September 2010 in track 442; 47 ascending images from January 2005 to September 2010 in track 170; and 51 descending images from May 2005 to September 2010 in track 120. The parameters of the three datasets are shown in Table 1. The spatial and temporal distributions are shown in Figure 1, and the coverage is shown in Figure 2.

GPS observation data are acquired from the Southern California Integrated GPS Network (SCIGN, <http://www.Scign.org> (accessed on 27 November 2021)) to verify with InSAR results. The SCIGN is one of the most densely distributed GPS networks in the world, but the spatial resolution is still low (>10 km) and unable to obtain high spatial resolution surface deformation information. InSAR technology shows its unique advantages in

the field of land deformation monitoring because of its large monitoring range, high measurement accuracy, and weather-independent characteristics.

Table 1. List of parameters for the three ENVISAT ASAR SAR datasets.

Track	442	170	120
Orbit direction	descending	descending	ascending
Temporal coverage	20051124–20101014	20050514–20100925	20050126–20100922
No. of images	33	51	47
Wavelength (m)	0.056	0.056	0.056
Incidence (degree)	22.8	22.6	22.8
Heading (degree)	−166.534	−166.527	−13.407
Polarization	VV	VV	VV

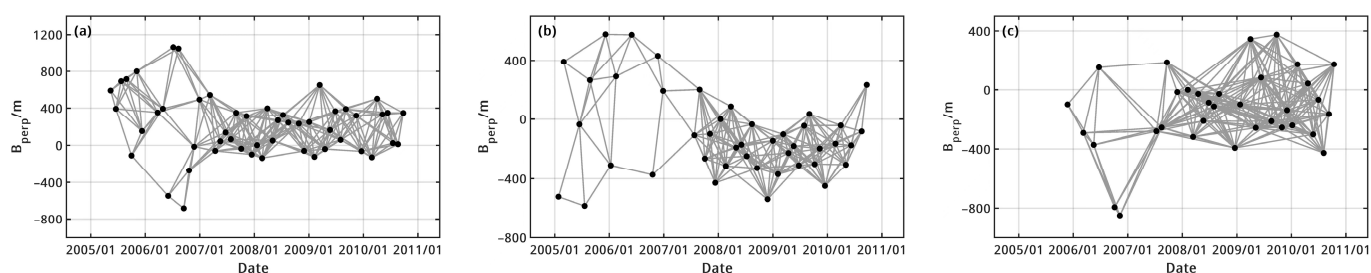


Figure 1. Illustration of temporal–spatial baseline distribution. (a) track 170; (b) track 120; (c) track 442.

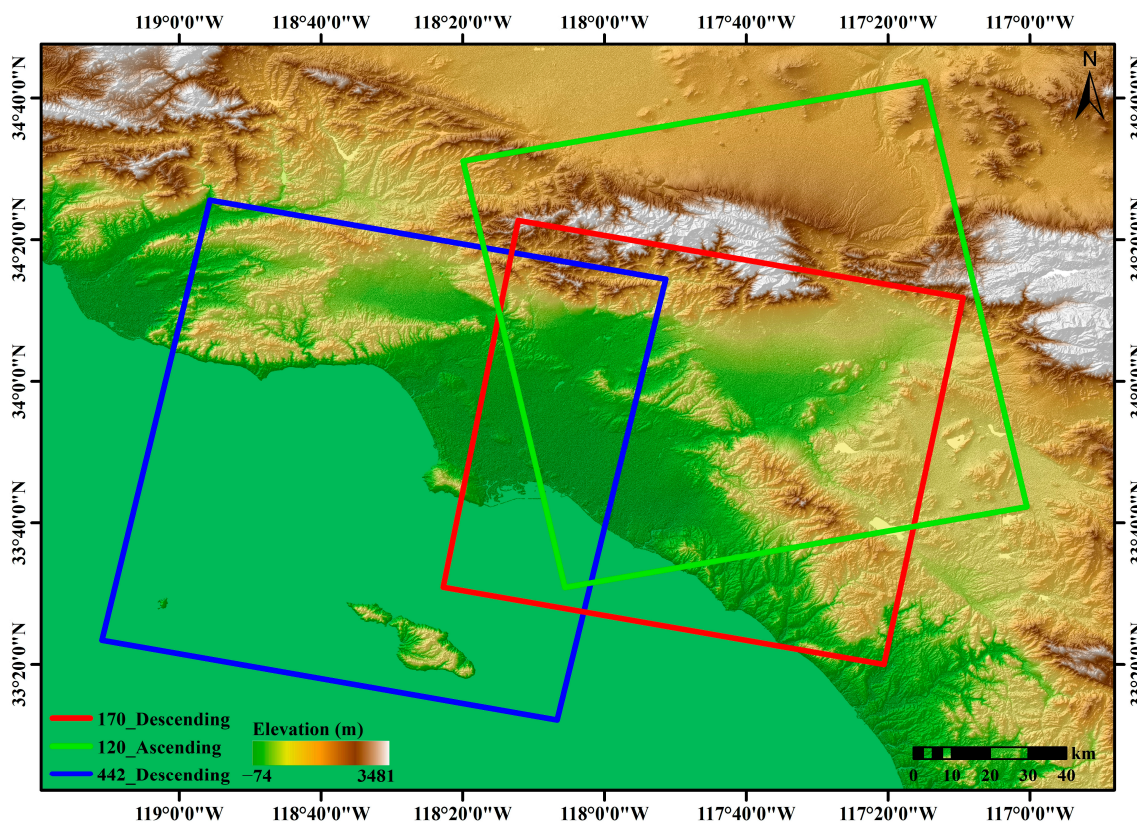


Figure 2. Coverage of three SAR datasets. Blue rectangle is track 442, red rectangle is track 170, and green rectangle is track 120. The background is SRTM DEM with a resolution of 30 m.

3. Methodology

3.1. SBAS-InSAR

Firstly, we use StaMPS/SBAS to process three datasets separately to obtain their respective deformation rates and the unwrapped interferograms [28,29].

Supposing interferograms are generated from $N + 1$ SAR images with a time interval from t_0 to t_N , the relationship between the unwrapped phase $\delta\phi^T = [\delta\phi_1 \cdots \delta\phi_M]$ and the phase of the SAR image $\phi^T = [\phi(t_0) \cdots \phi(t_N)]$ is expressed as [30]:

$$\delta\phi_k = \phi(t_j) - \phi(t_i) \quad (1)$$

In order to obtain a physical solution, the unknown parameters are represented by the mean phase rate [30]:

$$v^T = \left[v_1 = \frac{\phi_1}{t_1 - t_0}, \cdots, v_N = \frac{\phi_N - \phi_{N-1}}{t_N - t_{N-1}} \right] \quad (2)$$

Equations (1) and (2) are expressed as follows:

$$Bv = \delta\phi \quad (3)$$

Generally, a matrix B is decomposed by singular value decomposition (SVD) [30].

SRTM DEM with a resolution of 30 m is used to remove the terrain phase and flat phase. The reference point is selected at the ELSC station of the GPS network, and the interferograms and deformation rate are obtained and then geocoded, respectively.

3.2. USLS

Large-scale surface deformation event monitoring requires multiple paths to cover the whole study area [31]. While the imaging geometry and acquisition time of adjacent paths are different, the error distribution is also distinct, and the orbit trend error is the most obvious [32,33]. A unified simultaneous least squares (USLS) approach is applied to remove the deformation discontinuity between adjacent SAR image paths [34].

In order to link the deformation results obtained on the adjacent paths, the GPS stations are selected as the ground control points (shown as triangles in Figure 3), and measurement points (MP), such as rocks, buildings, etc., can be chosen as the tie points (shown as dots in Figure 3) in the common area.

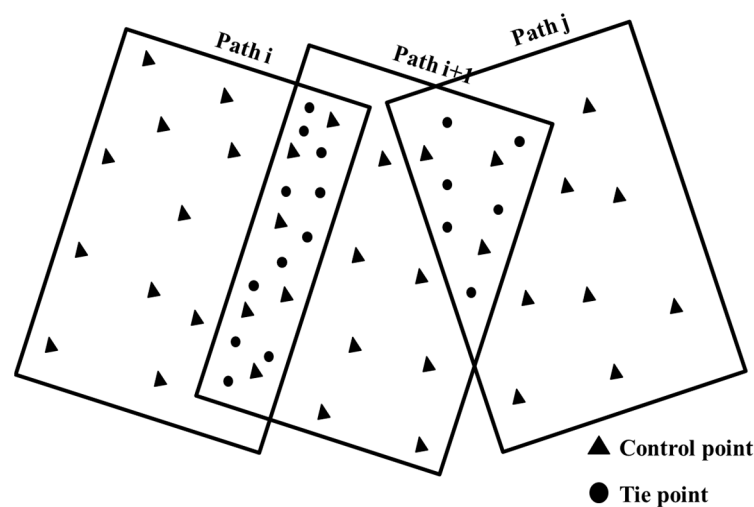


Figure 3. Velocity control points and tie points in multiple paths. Triangles and dots represent control points and tie points, respectively.

Assuming I_i and G_i are surface deformations of a control point from InSAR and GPS on path i :

$$I_i - G_i = a_{i,0} + a_{i,1}x_i + a_{i,2}y_i + a_{i,3}x_iy_i + a_{i,4}x_i^2 + a_{i,5}y_i^2 \quad (4)$$

Additionally, I_{i+1} and I_i are the InSAR deformations of tie points in the overlapping area between path $i + 1$ and i :

$$I_{i+1} - I_i = a_{i+1,0} + a_{i+1,1}x_i + a_{i+1,2}y_i + a_{i+1,3}x_iy_i + a_{i+1,4}x_i^2 + a_{i+1,5}y_i^2 - (a_{i,0} + a_{i,1}x_i + a_{i,2}y_i + a_{i,3}x_iy_i + a_{i,4}x_i^2 + a_{i,5}y_i^2) \quad (5)$$

Finally, the orbit trend is calculated with the estimated parameters $a_{i,0}, \dots, a_{i,5}$ and $a_{i+1,0}, \dots, a_{i+1,5}$, and the deformation result after orbit error correction is achieved [22].

Due to the different imaging geometry of multiple SAR satellite systems, the coordinate system and the reference datum of the deformation results are inconsistent. The unwrapping phase in the radar coordinate system is geocoded, so the measurements of the multi-path are located in the unified geographical coordinate system with longitude and latitude. In order to achieve the unification of reference datum, the reference points of different platforms are selected at the same location.

3.3. Different LOS Directions Transformation

The incidence angle and heading angle of SAR data from multiple azimuth directions are different, which leads to the inconsistency of the line of sight (LOS) direction, even if there are slight differences between adjacent paths. Therefore, the LOS measurements of different tracks are needed be unified into the same LOS direction.

The LOS unit vector of one path can be defined as follows [35]:

$$\mathbf{r} = \begin{bmatrix} r_{\text{east}} \\ r_{\text{north}} \\ r_{\text{up}} \end{bmatrix} = \begin{bmatrix} -\sin \theta \cos \alpha \\ \sin \theta \sin \alpha \\ \cos \alpha \end{bmatrix} \quad (6)$$

where θ is incidence angle and α is the satellite flight azimuth.

So, the transformation between different LOS directions is defined as:

$$d_2^{\text{los}} = d_1^{\text{los}} / (r_1^{\text{east}}r_2^{\text{east}} + r_1^{\text{north}}r_2^{\text{north}} + r_1^{\text{up}}r_2^{\text{up}}) \quad (7)$$

In this paper, we project the LOS deformation of tracks 120 and 442 onto the LOS direction of track 170.

The flow chart is shown in Figure 4.

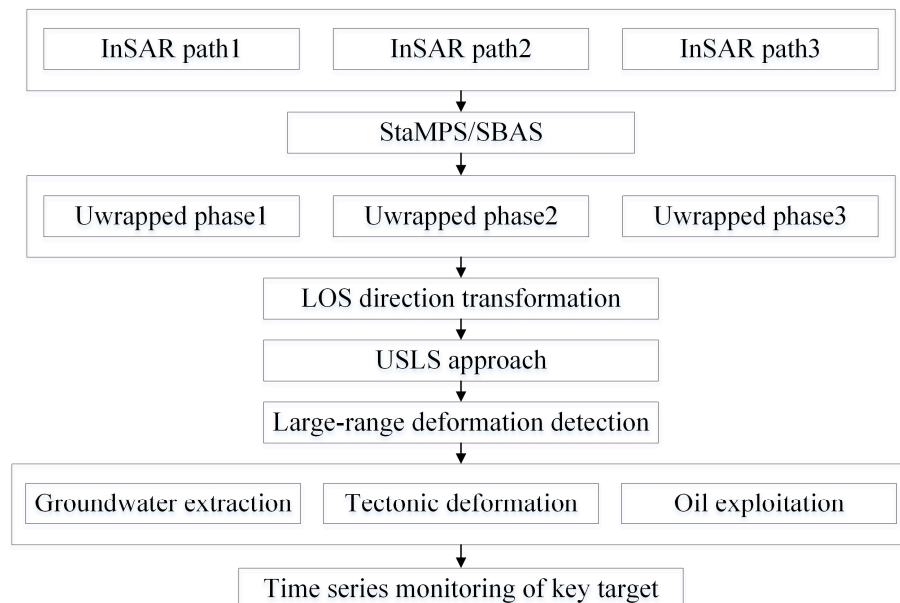


Figure 4. The flow chart of processing.

4. Result and Validation

4.1. Large-Range Deformation Detection Results

The USLS approach is applied to remove the deformation discontinuity between three paths (as shown in Figure 5a), and the corrected annual deformation rate of Southern California is shown in Figure 5b. The seam line in Figure 5a has been avoided, and the velocity discontinuity along profiles 1 and 2 in Figure 6a,b has disappeared. The resulting seamless velocity in Figure 5b and the continuous velocity profile in Figure 6c,d suggest that the USLS approach minimizes the discrepancy of velocity measurements between adjacent paths and enhances the consistency of velocity measurements. Results appeared continuous after correction, and this area has regional deformation characteristics: surface subsidence is mainly related to groundwater extraction and oil exploitation; the uplift trend is caused by changes in injection and declining oilfield operations [26]; and uneven deformation affected by faults, meanwhile, occur in many regions.

However, from the InSAR and GPS monitoring results, we find that Southern California has obvious periodic deformation characteristics, so the large-scale deformation rate results obtained by the USLS method are applied to the analysis of the deformation magnitude and trend characteristics. It can be used to investigate the deformation area but cannot fully reflect the temporal deformation evolution.

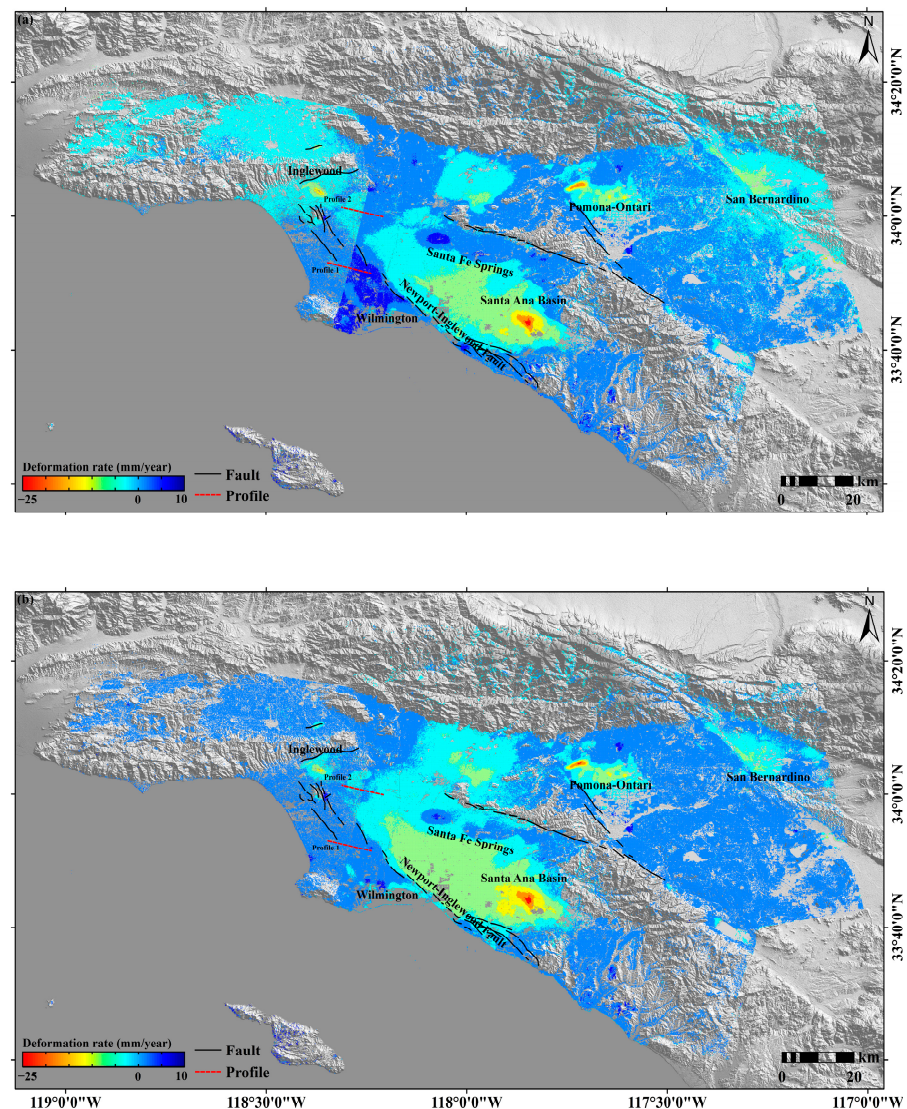


Figure 5. Annual deformation rate of Southern California. (a) is before correction; (b) is after correction. The background is SRTM DEM with a resolution of 30 m.

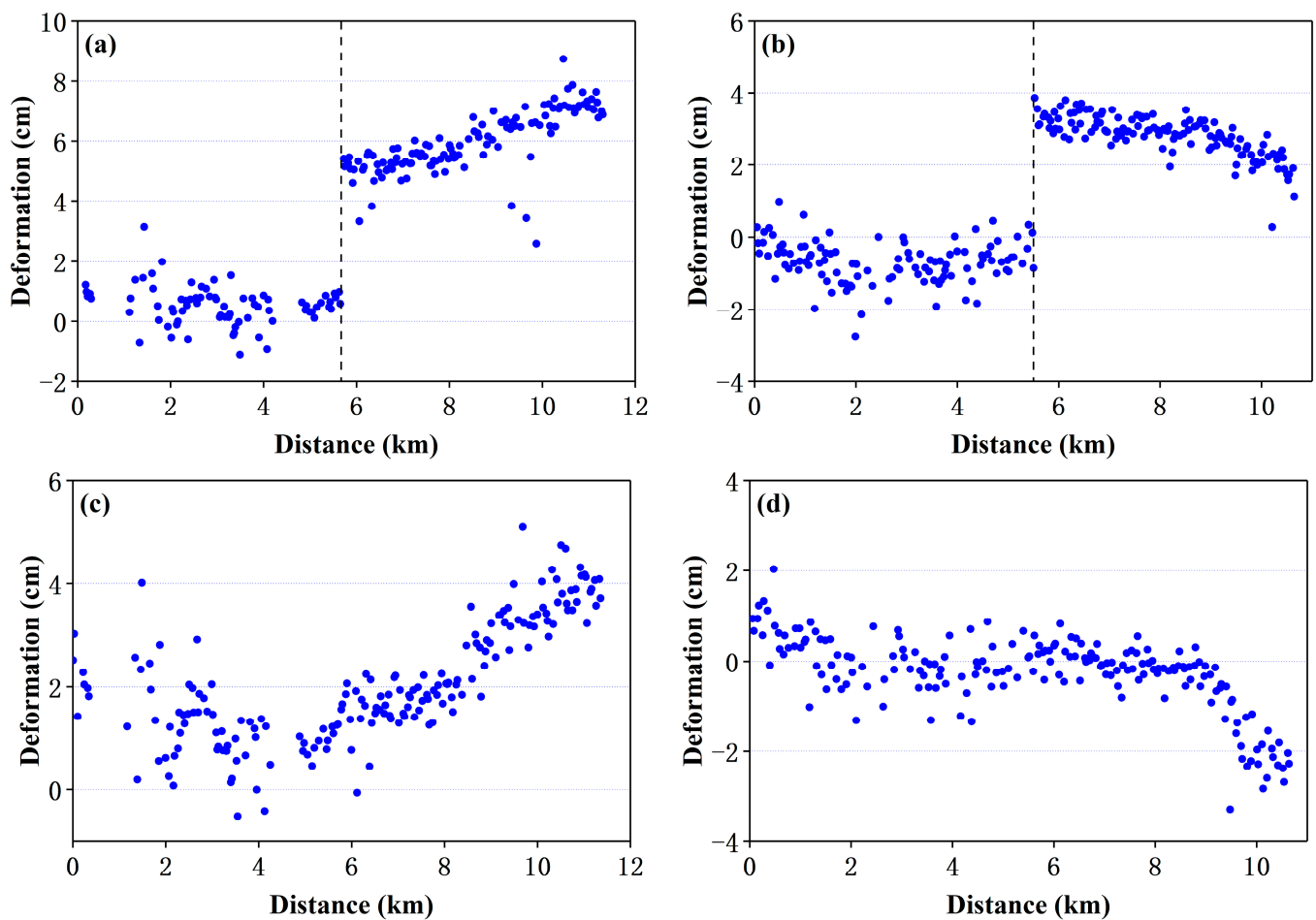


Figure 6. Velocity from 2005 to 2010 along Profiles 1 and 2 shown in Figure 5. (a,b) are the results before correction; (c,d) are the results after correction by USLS.

4.2. Various Deformation Patterns Monitoring

InSAR and GPS technologies are utilized to monitor land subsidence, active faults, and oil fields and finding out and mastering the magnitude, range, and characteristics of ground deformation in Southern California.

4.2.1. Groundwater Extraction and Recharge

In order to ensure the safety of drinking water, food security, and economic and social development, many urban areas have to develop and utilize groundwater on a large scale. With the rapid development of urban construction, the need for water for production and living is also increasing. Because of the shortage of water resources, the situation of short supply is becoming more and more obvious. Shallow groundwater has been unable to meet the needs of human beings, resulting in the development and utilization of deeper groundwater resources. Urban construction and excessive exploitation of groundwater are the main causes of land deformation. Land deformation will not only affect and destroy the artificial target and construction facilities but also change the groundwater environment in turn. A large number of cities relying on groundwater for both production and living have experienced different degrees of land deformation, and the more developed the economy, the more obvious the land deformation and the greater the economic losses suffered.

Land deformation caused by groundwater exploitation is directly related to groundwater level and indirectly related to precipitation. As it is difficult to obtain accurate groundwater level data, we acquired the precipitation data in this area from the NASA website (<https://pmm.nasa.gov/precipitation-measurement-missions> (accessed on 5 De-

ember 2021)) to verify the relationship between deformation time series and monthly precipitation. Figure 7 shows the GPS and InSAR monitoring results at four GPS stations.

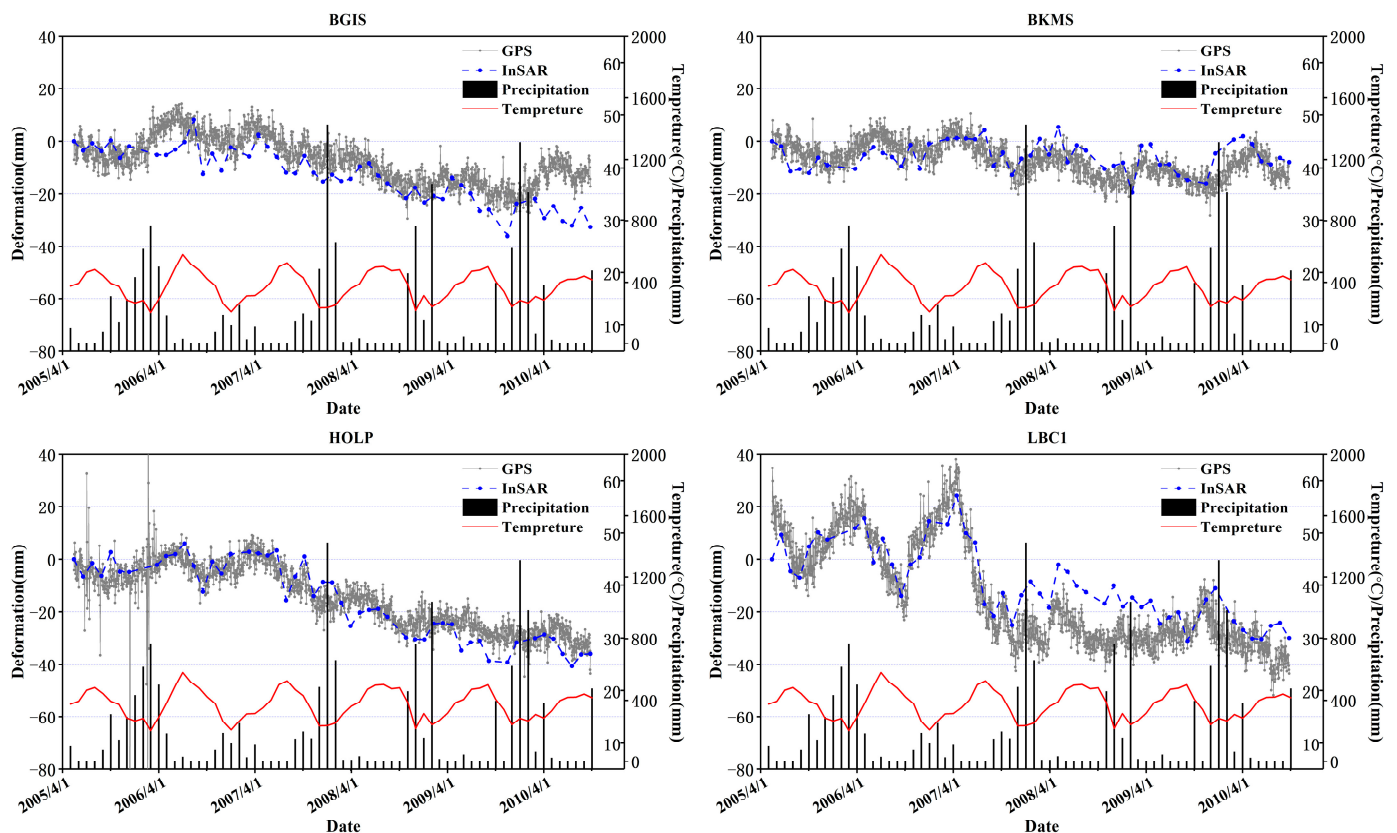


Figure 7. Time series deformation of GPS and InSAR monitoring results. Gray points connected by the gray solid line represent the GPS observation data projected on LOS direction of track 170 ASAR dataset. Blue points connected by the blue dashed line display time-series measurements of InSAR monitoring results. Grey bar chart illustrates the monthly cumulative precipitation. Red solid line illustrates the monthly temperature.

There is an inverse correlation between temperature and precipitation. Temperature causes thermal expansion and cold contraction of the surface in the horizontal direction, but it is not the main reason for the surface fluctuation. An obvious correlation between the fluctuation of surface deformation and the precipitation period was found, but the periodic change of deformation lagged behind the precipitation; that is to say, when the precipitation increases, it will cause the rise of groundwater level, while the uplift of surface deformation has a hysteresis effect, and the hysteresis effect is inconsistent at different measurement points due to different surface fracture degree, water permeability, surface coverage, and strength in various areas. Taking the observation data of the BKMS GPS monitoring station as an example, the cross wavelet transform [36] is applied to analyze the relationship between InSAR deformation and precipitation (as shown in Figure 8), and the closed thick, black, solid line is the 95% confidence level contour line. The thin, black, solid line represents the cone of influence (COI). The black arrow reflects the phase relationship of the two-time series involved in the cross wavelet transform and wavelet coherence analysis: if the arrow direction is specified to the right, it means that the two phases are the same, and the left is opposite; if the arrow goes upward, it indicates 1/4 cycle of precipitation ahead of land deformation, then downward indicates 1/4 cycle of land deformation ahead of precipitation. The results indicate a strong correlation between InSAR deformation and precipitation, and the deformation lags behind precipitation by three to four months.

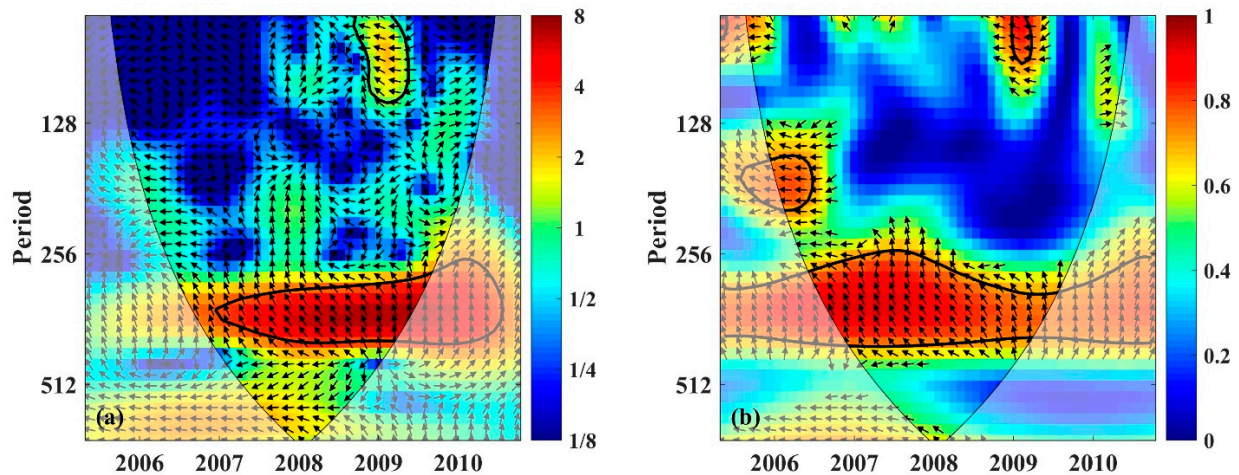


Figure 8. Cross wavelet transform (a) and squared wavelet coherence (b) of the InSAR deformation and precipitation time series. The 5% significance level against red noise is shown as a thick contour.

Figure 9 displays the time series results (Figure 9d–f) of three subsidence basins (Figure 9a is the Santa Ana Basin, Figure 9b is the Pomona–Ontar Basin, and Figure 9c is the San Bernardino Basin). The result of the deformation rate extracted along the profile in Figure 9a–c is shown in Figure 9g–i. We can find that the exploitation of groundwater will cause strong land subsidence, especially in the deformation center, where the maximum deformation rate exceeds 20 mm/year in the Santa Ana Basin and the Pomona–Ontar Basin and the cumulative deformation reaches -10 cm. The settlement is generally funnel-shaped, and deformation time series and precipitation also have the characteristics of strong correlation and hysteresis effect. It shows that the precipitation does not directly lead to surface deformation but first causes the change of groundwater level, and the rise and fall of groundwater level then trigger the fluctuation of surface deformation, which is similar to the precipitation period.

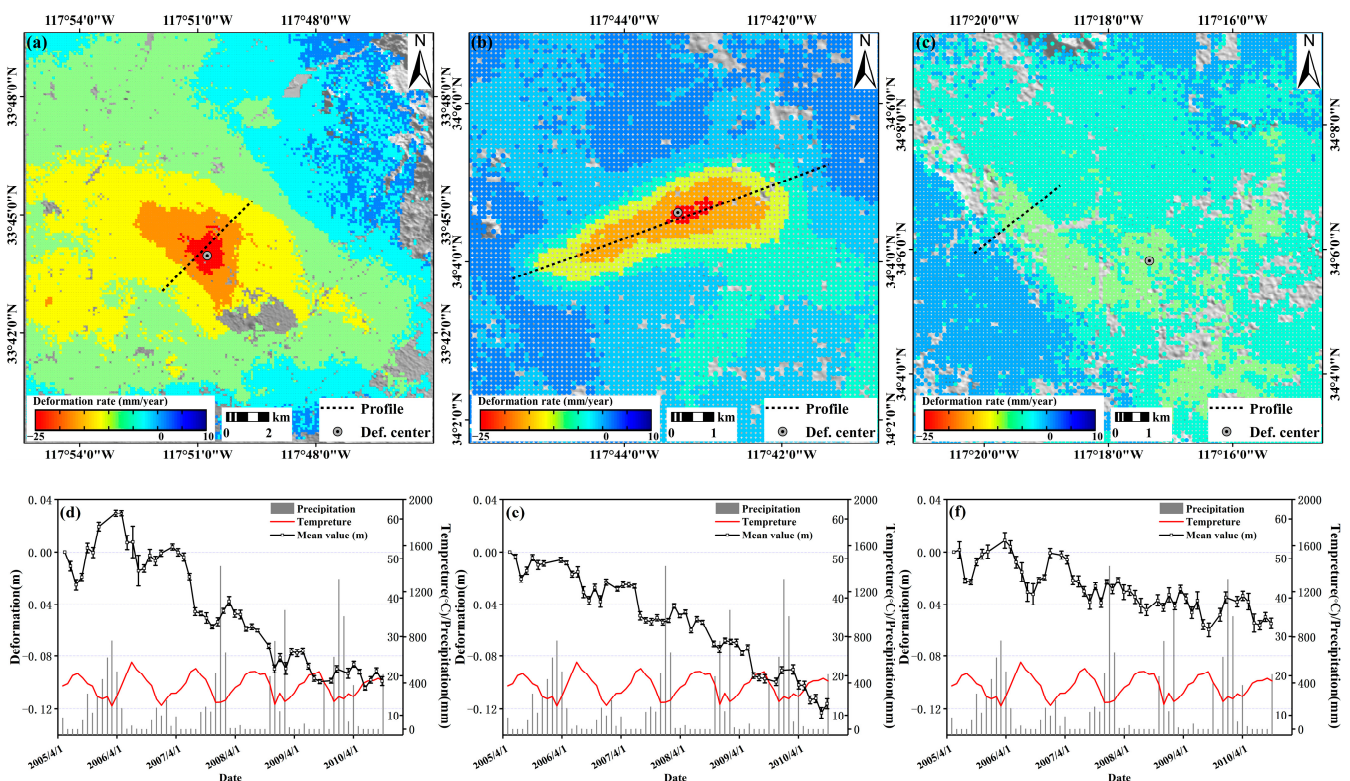


Figure 9. Cont.

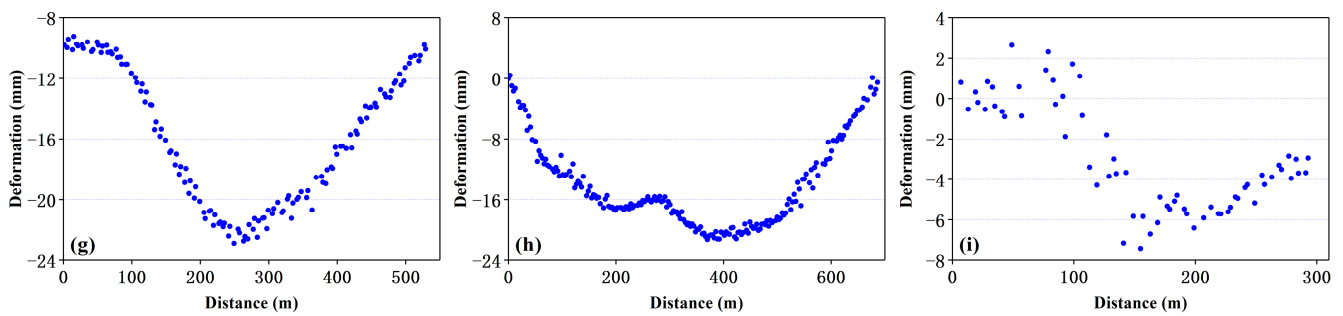


Figure 9. Land deformation rate and time series of three subsidence area. (a–c) is Santa Ana Basin, Pomona–Ontar Basin, and San Bernardino Basin; (d–f) Corresponding time series of deformation center; (g–i) the result of deformation rate that is extracted along the profile.

4.2.2. The Deformations by the Other Factors

The geological structure is complex in Southern California, and many faults crisscross. Where the faults pass, the ground and underground buildings will be easily damaged, especially the water and gas supplies, and the drainage system laid underground in the city is seriously threatened. The uneven settlement also causes the buildings and cultural relics to be tilted and wrecked, which in turn accelerates the fault activity. These disasters not only affect the planning and layout of the city, the effective use of land, and the development of underground space, but also endanger the safety of all kinds of buildings and bring difficulties to the lives of urban residents. The edge of the land deformation area is often located at the side of faults, and its magnitude is affected by the constraints of faults activities. Figure 10 displays the inhomogeneous deformation on both sides of the faults.

Figure 10a,b have similar deformation characteristics, the ground deformation is divided into three sections by faults: homogeneous deformation area at both sides, inhomogeneous deformation area in the middle, and the two sides across the faults appear different deformation rates (the deformation difference in Newport–Inglewood Fault is about 6 mm, while it is 4 mm near San Bernardino Basin), the above-ground buildings and underground facilities in the middle section are easy to break, tilt, misplace, even collapse and damage under the uneven stress.

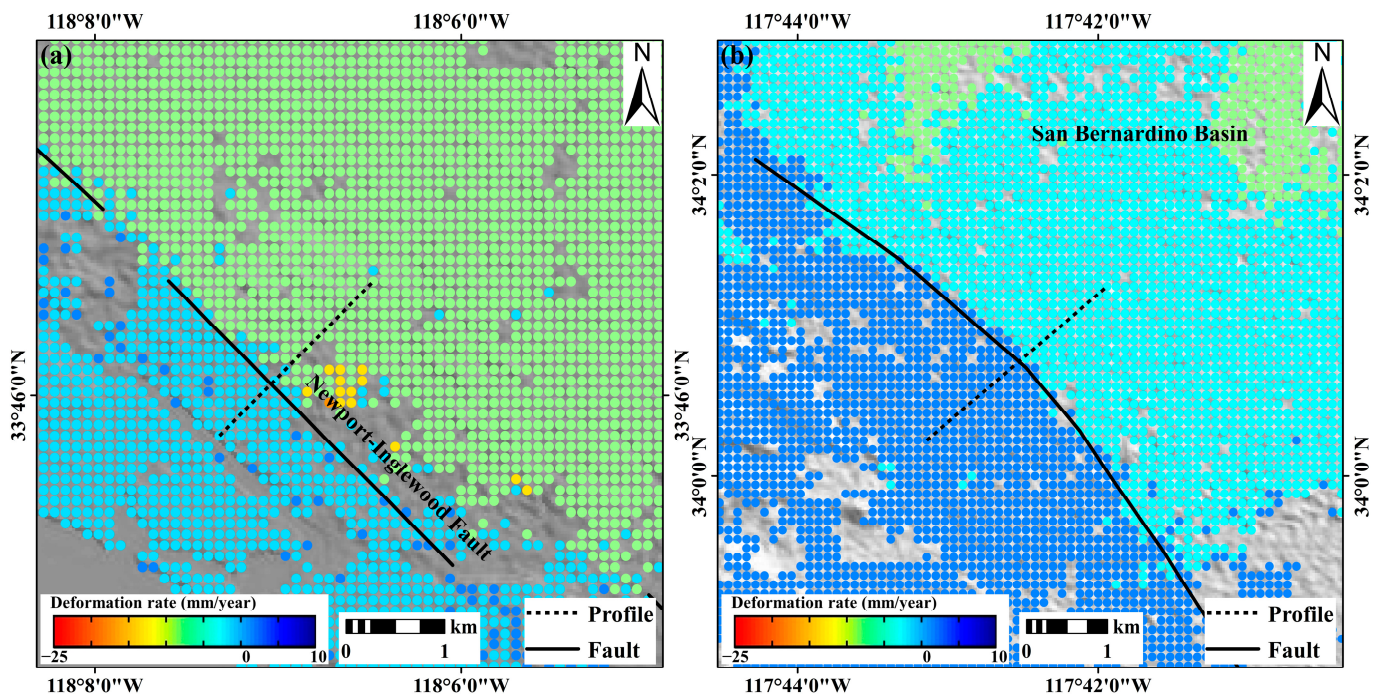


Figure 10. Cont.

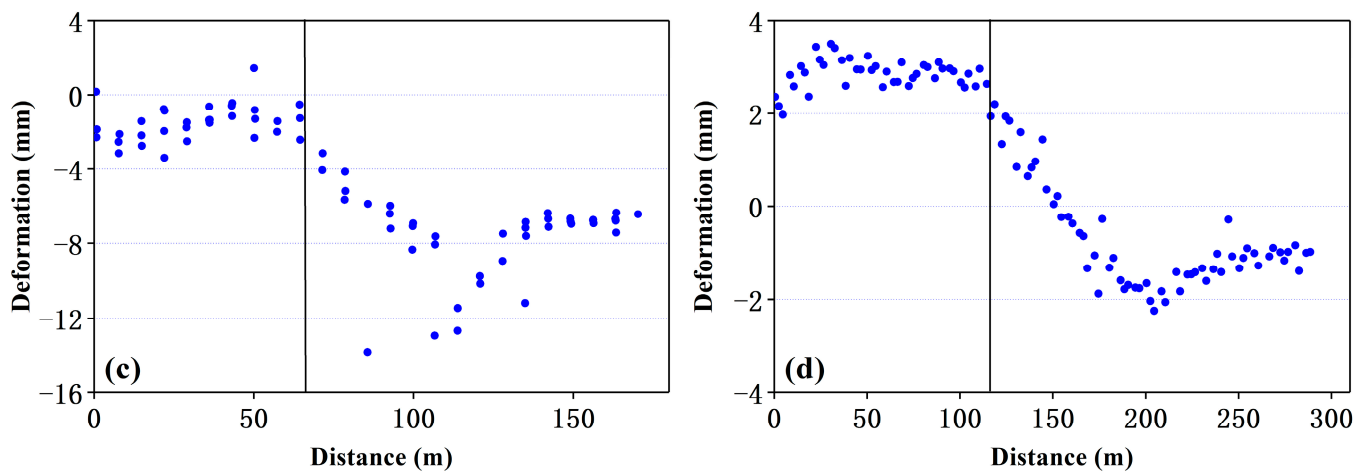


Figure 10. Inhomogeneous deformation of structural faults. (a) is part of Newport–Inglewood Fault and (b) is near San Bernardino Basin; (c,d) is the corresponding deformation rate extracted along the profile (black solid line indicates fault location).

Overexploitation of underground liquid or gas will lead to a decrease in pore pressure, an increase in effective stress, and the formation compaction. The damage caused by ground deformation caused by overexploitation is very serious and will ruin surface or underground structures. In coastal areas, it will also cause adverse consequences such as seawater intrusion, failure of harbor facilities, etc.

Southern California is rich in mineral resources and numerous oil fields, such as the Inglewood Oilfield, the Santa Fe Springs Oilfield, and the Wilmington Oilfield. The main surface deformation area occurs in the oil field production region, which is approximately elliptical. The deformation rate field and corresponding results extracted along the profiles of the Inglewood oilfield, Santa Fe Springs oilfield, and Wilmington oilfield are shown in Figure 11. Three oilfields show different land deformation patterns. Inglewood oilfield is characterized by a subsidence signal with two settlement centers, and the maximum deformation is more than 12 mm/year. The Santa Fe Springs oilfield shows uplift deformation; the largest deformation location is at the center position of the oilfield, at about 6 mm/year. There are two types of deformation patterns in the Wilmington oilfield: west subsidence and east uplift. The maximum deformation rate of the settlement area is 4 mm/year, while that of the lifting area is 8 mm/year.

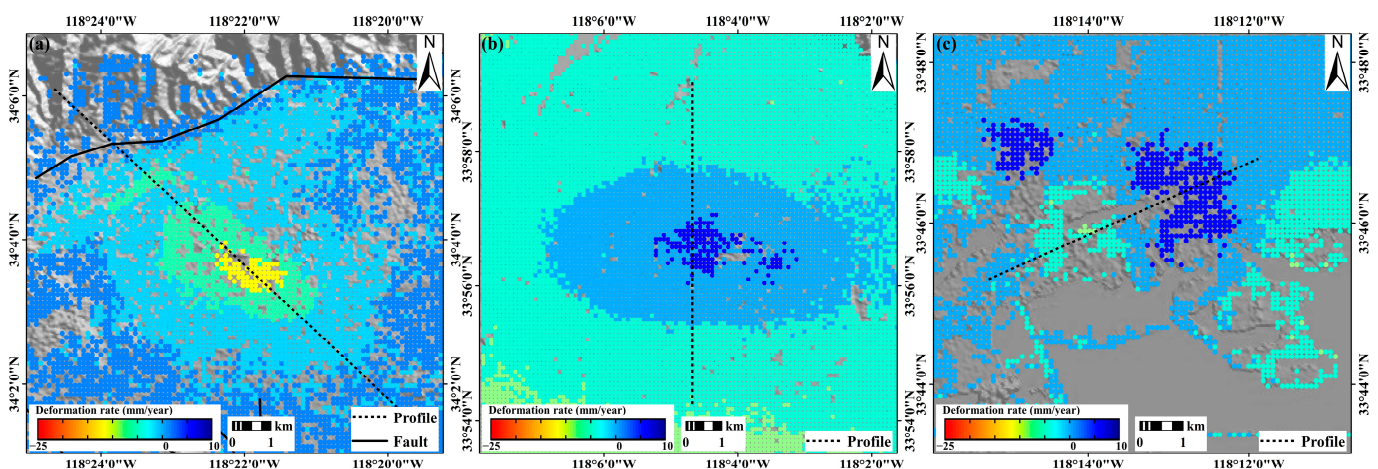


Figure 11. Cont.

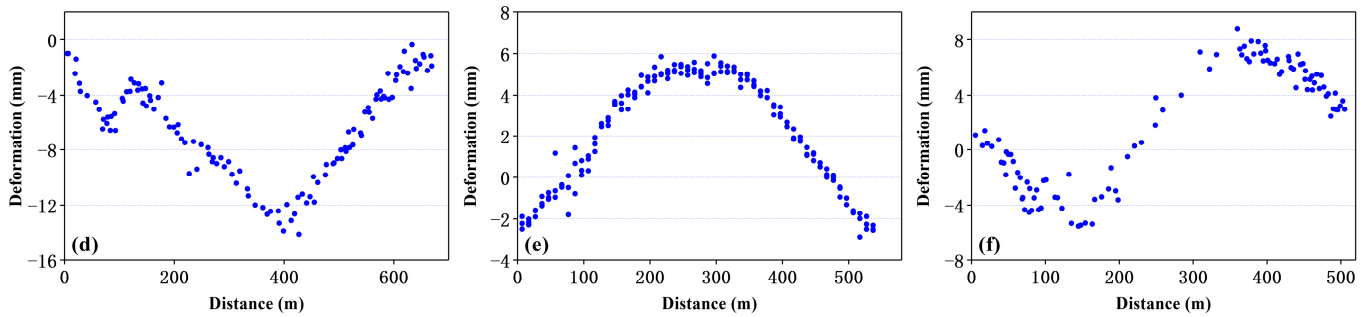


Figure 11. Deformation field of (a) Inglewood oilfield; (b) Santa Fe Springs oilfield; and (c) Wilmington oilfield. (d–f): the corresponding deformation rate extracted along the profile.

From the GPS and InSAR observation data monitored by BKMS near the Santa Fe Springs oilfield, the linear deformation trend around the oilfield is not obvious but mainly characterized by periodic fluctuations. The subsidence and uplift in this area are directly related to the extraction and reinjection of underground materials (oil, gas, etc.) [18].

4.3. Validation with GPS Observation Data

From Figure 5, we can see that SCIGN has densely distributed GPS stations, but its spatial resolution is still very low compared with InSAR measurement points. We obtained observation data from 49 GPS monitoring stations, and 25 stations (except that no effective InSAR measurement points are identified around some GPS stations) are utilized for mutual verification with InSAR results (as shown in Figure 12). The GPS three-dimensional (3-D) deformation is projected in the LOS direction of InSAR. The comparison with GPS monitoring data shows that the deformation measurement accurately reflects the surface deformation fluctuation, and the periodicity is consistent.

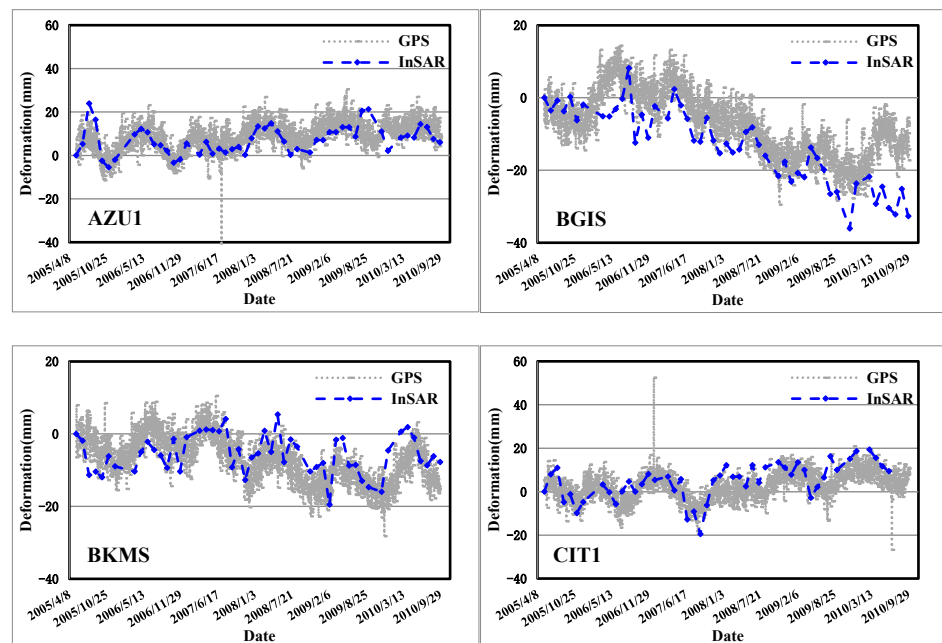


Figure 12. Cont.

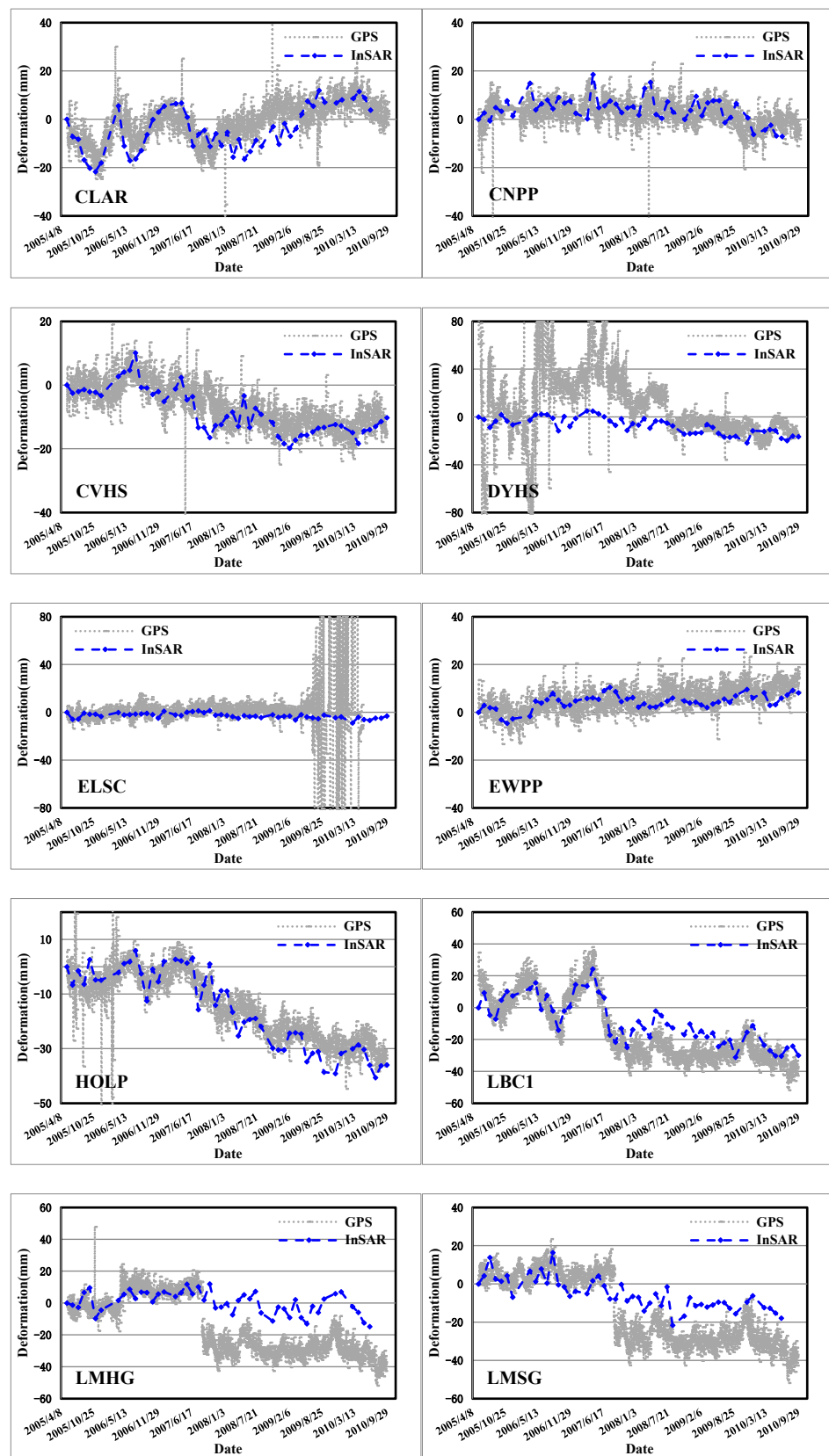


Figure 12. Cont.

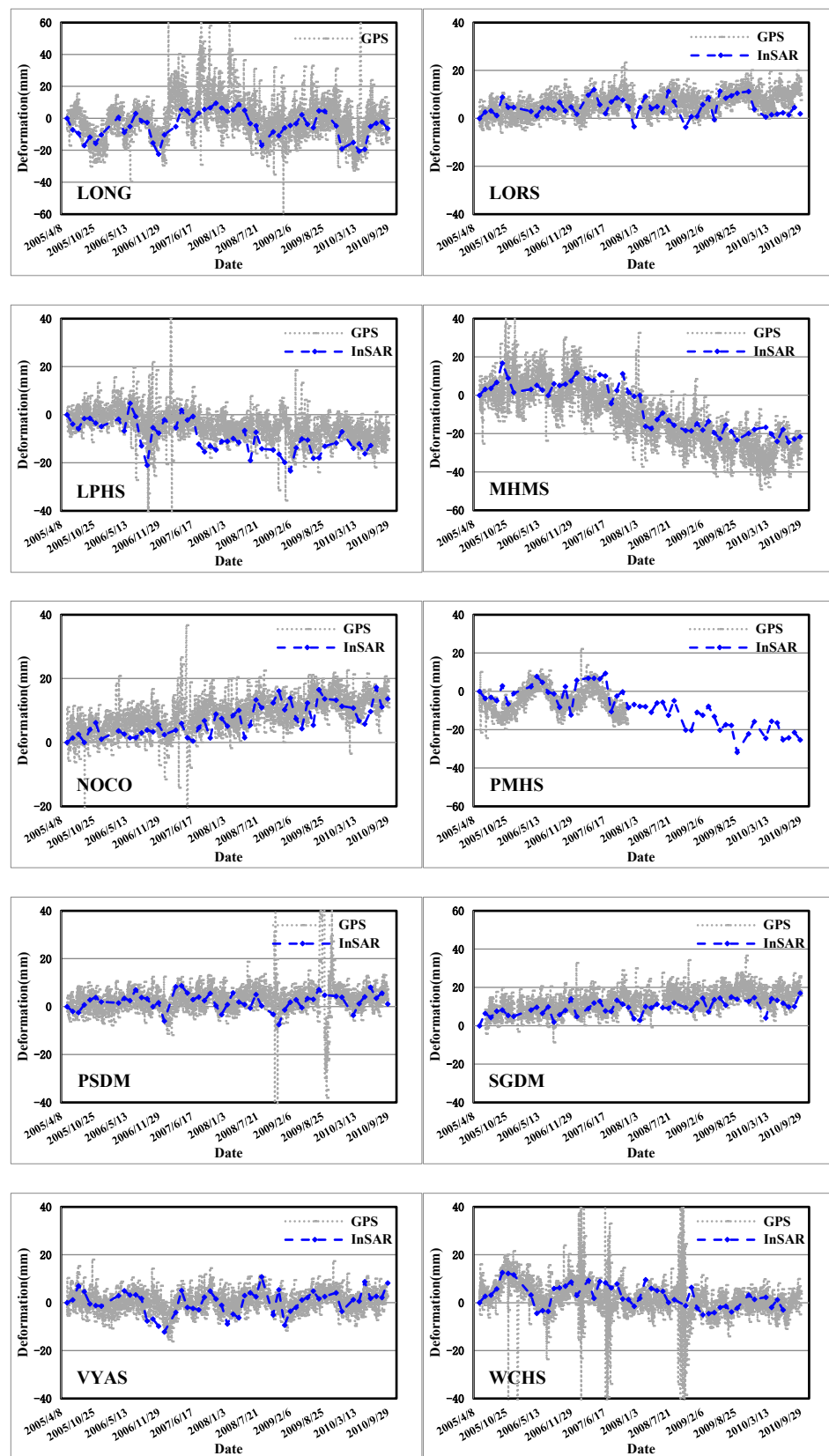


Figure 12. Cont.

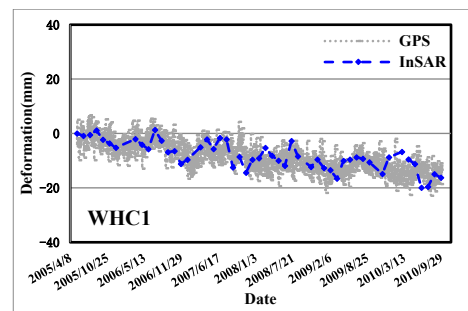


Figure 12. Comparisons of LOS time series from InSAR results (blue dashed line) and GPS monitoring data (grey dot line).

5. Discussion

Multi-path SAR datasets are usually acquired from different orbits even if the adjacent track has a slight difference in LOS direction, the fusion of multi-path datasets should be corrected to the same LOS direction. The three datasets used in this paper have almost the same temporal coverage, so the annual deformation rate can reflect the general deformation trend during the temporal period, and the USLS method is applied to remove deformation discontinuity between adjacent SAR image paths. The deformation discontinuity between adjacent SAR image paths is generally considered an orbit trend error [32,33]. The difference in deformation results in multi-paths that is inverted by the USLS approach to establishing a polynomial model. If the difference is complex, this approach will no longer be applicable. In addition, GPS monitoring stations are selected as the ground control points for areas with no or few control points, this approach has limitations when only using the tie points.

Due to the lack of groundwater level data, it is impossible to directly prove the relationship between land deformation and groundwater. However, we find that deformation fluctuation and precipitation period have strong correlation and hysteresis effect. This will help to analyze the impact of disastrous climate (rainstorms, heavy rainfall, etc.) on surface deformation and strengthen the observation and prevention of disastrous climate.

Three C-band ENVISAT ASAR datasets were collected due to the active deformation in Southern California during this period. Sufficient monitoring data, such as ALOS-1, ENVISAT, and GPS monitoring data, can be used for mutual comparison and verification [8]. So, the fusion of multi-path ENVISAT SAR data is aimed to compensate for the historical deformation of Southern California and analyze the temporal evolution regularity and spatial distribution characteristics of surface deformation. The data used in this experiment are all C-band, which are sensitive to temporal decorrelation in vegetation-covered areas. There are not enough measurement points identified in mountainous areas with dense vegetation, and the deformation information cannot be obtained.

Two stacks of C-band Sentinel-1 (S1-desc and S1-asc) images were collected to study the current deformation phenomenon in Southern California [37]; however, the atmospheric propagation delay is obvious in this area, so a new approach of adaptive fusion of multi-source tropospheric delay (AFMTD) estimates derived from multiple models is proposed for InSAR tropospheric delay correction. More monitoring technologies and observation data will be available in the future to study the deformation mechanisms of this typical experimental area in Southern California.

6. Conclusions

Multiple paths SAR datasets were collected to investigate the surface land deformation using the USLS approach. The large-scale surface deformation field of Southern California was achieved from 2005 to 2010. Various deformation patterns are monitored and analyzed.

First, groundwater exploitation is the main cause of land deformation in Southern California. In the deformation center, the maximum deformation rate exceeds 20 mm/year in the Santa Ana Basin and Pomona–Ontar Basin. The settlement is generally funnel-

shaped, and the fluctuation of surface deformation has a hysteresis effect compared with precipitation.

Second, the magnitude of deformation on different sides of the structural fault is usually inconsistent, resulting in uneven deformation. Meanwhile, the edge of land deformation area is often located at the side of faults, and the faults control the location and extension of land deformation. Active faults are a great threat to both the ground buildings and the underground infrastructure. The ground buildings on the fault will crack, topple, or even tumble, while the underground facilities will be dislocated and broken.

Third, Southern California is rich in mineral resources and has numerous distributed oil fields. Due to the change of the underground material, the surface of the oil mining area will appear to have an elliptical deformation area. However, from the time series analysis, Inglewood oilfield shows a subsidence signal, Wilmington oilfield shows an uplift deformation, and Santa Fe Springs has both.

In this paper, the multi-path SAR data is utilized to obtain the large-scale deformation field in Southern California, and the time series of the key concern areas are analyzed. Such information should be helpful in decision-making in land deformation mitigation and water resource management.

Author Contributions: Methodology, Y.S. and S.L.; software, X.W.; resources, F.W.; data curation, H.Z. and D.Y.; writing—original draft, M.A.; writing—review & editing, L.W. All authors have read and agreed to the published version of the manuscript.

Funding: This work was financially supported by the National Natural Science Foundation of China (Grant No. 42071453), the Fund of the National Key Laboratory of Science and Technology on Remote Sensing Information and Imagery Analysis, the Beijing Research Institute of Uranium Geology (Grant No. 6142A01210407), the Fundamental Research Funds for the Central Universities (Grant No. N2201020), and the Geological Disaster Survey Project of Liaoning Province (Grant No. 2022020700179).

Data Availability Statement: No new data were created or analyzed in this study. Data sharing is not applicable to this article.

Acknowledgments: ENVISAT ASAR data were provided by the European Space Agency (ESA) through the framework of the Sino-EU Dragon Project (ids 32365-4 and 58029). GPS data were provided by the Southern California Integrated GPS Network (SCIGN).

Conflicts of Interest: The authors declare no conflict of interest.

References

- Bamler, R.; Hartl, P. Synthetic aperture radar interferometry. *Inverse Probl.* **1998**, *14*, R1–R54. [[CrossRef](#)]
- Massonnet, D.; Feigl, K.L. Radar interferometry and its application to changes in the Earth's surface. *Rev. Geophysical.* **1998**, *36*, 441–500. [[CrossRef](#)]
- Ferretti, A.; Monti, G.A.; Prati, C.; Rocca, F.; Massonnet, D. *InSAR Principles: Guidelines for SAR Interferometry Processing and Interpretation*; ESA Publications; ESTEC: Noordwijk, The Netherlands, 2007; pp. 24–29.
- Moreira, A.; Prats-Iraola, P.; Younis, M.; Krieger, G.; Hajnsek, I.; Papathanassiou, K.P. A tutorial on synthetic aperture radar. *IEEE Geosci. Remote Sens. Mag.* **2013**, *1*, 6–43. [[CrossRef](#)]
- Lu, Z.; Dzurisin, D. *InSAR Imaging of ALEUTIAN Volcanoes: Monitoring a Volcanic Arc from Space*; Springer Praxis Books; Springer: Berlin/Heidelberg, Germany, 2014; Volume 8, pp. 1778–1786.
- Nádudvari, Á. Using radar interferometry and SBAS technique to detect surface subsidence relating to coal mining in Upper Silesia from 1993–2000 and 2003–2010. *Environ. Socio-Econ. Stud.* **2016**, *4*, 24–34. [[CrossRef](#)]
- Przyłucka, M.; Kowalski, Z.; Perski, Z. Twenty years of coal mining-induced subsidence in the Upper Silesia in Poland identified using InSAR. *Int. J. Coal. Sci. Technol.* **2022**, *9*, 86. [[CrossRef](#)]
- Dang, V.K.; Nguyen, T.D.; Dao, N.H.; Duong, T.L.; Dinh, X.V.; Weber, C. Land subsidence induced by underground coal mining at Quang Ninh, Vietnam: Persistent scatterer interferometric synthetic aperture radar observation using Sentinel-1 data. *Int. J. Remote Sens.* **2021**, *42*, 3563–3582. [[CrossRef](#)]
- Wei, L.; Liu, S.; Mao, Y.; Wang, R.; Wu, L.; Xu, J. Joint application of DInSAR and ground measurements: A case study on dump stability analysis. In *IGARSS 2016–2016 IEEE International Geoscience and Remote Sensing Symposium*; IEEE: New York, NY, USA, 2016.
- Qin, X.; Zhang, L.; Yang, M.; Luo, H.; Liao, M.; Ding, X. Mapping surface deformation and thermal dilation of arch bridges by structure-driven multi-temporal DInSAR analysis. *Remote Sens. Environ.* **2018**, *216*, 71–90. [[CrossRef](#)]

11. Wang, R.; Yang, T.; Yang, M.; Liao, M.; Lin, J. A safety analysis of elevated highways in Shanghai linked to dynamic load using long-term time-series of InSAR stacks. *Remote Sens. Lett.* **2019**, *10*, 1133–1142. [[CrossRef](#)]
12. Qin, X.; Zhang, L.; Ding, X.; Liao, M.; Yang, M. Mapping and Characterizing Thermal Dilation of Civil Infrastructures with Multi-Temporal X-Band Synthetic Aperture Radar Interferometry. *Remote Sens.* **2018**, *10*, 941. [[CrossRef](#)]
13. Ketelaar, V.B. *Satellite Radar Interferometry: Subsidence Monitoring Techniques*; Environmental Science; Springer: Berlin/Heidelberg, Germany, 2009.
14. Gabriel, A.K.; Goldstein, R.M.; Zebker, H.A. Mapping small elevation changes over large areas: Differential radar interferometry. *J. Geophys. Res.* **1989**, *94*, 9183–9191. [[CrossRef](#)]
15. Massonnet, D.; Holzer, T.; Vadon, H. Land subsidence caused by the East Mesa geothermal field, California, observed using SAR interferometry. *Geophys. Res. Lett.* **1997**, *24*, 901–904. [[CrossRef](#)]
16. Ferretti, A.; Prati, C.; Roesa, F. Nonlinear subsidence rate estimation using permanent scatterers in differential SAR interferometry. *IEEE Trans. Geosci. Remote Sens.* **2000**, *38*, 2202–2212. [[CrossRef](#)]
17. Bawden, G.W.; Thatcher, W.; Stein, R.S.; Hudnut, K.W.; Peltzer, G. Tectonic contraction across Los Angeles after removal of groundwater pumping effects. *Nature* **2001**, *412*, 812–815. [[CrossRef](#)] [[PubMed](#)]
18. Zhang, L.; Lu, Z.; Ding, X.L.; Jung, H.S.; Feng, G.C.; Lee, C.W. Mapping ground surface deformation using temporarily coherent point SAR interferometry: Application to Los Angeles Basin. *Remote Sens. Environ.* **2012**, *117*, 429–439. [[CrossRef](#)]
19. Hu, J.; Li, Z.W.; Ding, X.L.; Zhu, J.J.; Sun, Q. Spatial-temporal surface deformation of Los Angeles over 2003–2007 from weighted least squares DInSAR. *Int. J. Appl. Earth Obs. Geoinf.* **2013**, *21*, 484–492. [[CrossRef](#)]
20. Ao, M.; Zhang, L.; Liao, M.S.; Zhang, L. Deformation Monitoring with Adaptive Integration of Multi-Source InSAR Data Based on Variance Component Estimation. *Chin. J. Geophys.* **2020**, *63*, 2901–2911.
21. Davis, T.L.; Namson, J.; Yerkes, R.F. A cross section of the Los Angeles area: Seismically active fold and thrust belt, the 1987 Whittier Narrows Earthquake and earthquake hazard. *J. Geophys. Res.* **1989**, *94*, 9644–9664. [[CrossRef](#)]
22. Hauksson, E. Seismotectonics of the Newport-Inglewood fault zone in the Los Angeles Basin, southern California. *Bull. Seismol. Soc. Am.* **1987**, *77*, 539–561. [[CrossRef](#)]
23. Hauksson, E.; Jones, L.M. The 1987 Whittier Narrows earthquake sequence in Los Angeles, southern California: Seismological and tectonic analysis. *J. Geophys. Res.* **1989**, *94*, 9569–9589. [[CrossRef](#)]
24. Hauksson, E.; Jones, L.M.; Hutton, K. The 1994 Northridge earthquake sequence in California—Seismological and tectonic aspects. *J. Geophys. Res. Solid Earth* **1995**, *100*, 12335–12355. [[CrossRef](#)]
25. Watson, K.M.; Bock, Y.; Sandwell, D.T. Satellite interferometric observations of displacements associated with seasonal groundwater in the Los Angeles basin. *J. Geophys. Res. Solid Earth* **2002**, *107*, 2074. [[CrossRef](#)]
26. Lu, Z.; Danskin, W.R. InSAR analysis of natural recharge to define structure of a ground-water basin, San Bernardino, California. *Geophys. Res. Lett.* **2001**, *28*, 2661–2664. [[CrossRef](#)]
27. Xu, W.B.; Li, Z.W.; Ding, X.L.; Wang, C.C.; Feng, G.C. Application of small baseline subsets D-InSAR technology to estimate the time series land deformation and aquifer storage coefficients of Los Angeles area. *Chin. J. Geophys.* **2012**, *55*, 452–461.
28. Hooper, A.; Zebker, H.; Segall, P.; Kampes, B. A new method for measuring deformation on volcanoes and other natural terrains using InSAR persistent scatterers. *Geophys. Res. Lett.* **2004**, *31*, 1–5. [[CrossRef](#)]
29. Hooper, A. A multi-temporal InSAR method incorporating both persistent scatterer and small baseline approaches. *Geophys. Res. Lett.* **2008**, *35*, 96–106. [[CrossRef](#)]
30. Berardino, P.; Fornaro, G.; Lanari, R.; Sansosti, E. A new algorithm for surface deformation monitoring based on small baseline differential SAR interferograms. *Geosci. Remote Sens. IEEE Trans.* **2002**, *40*, 2375–2383. [[CrossRef](#)]
31. Sun, H.; Zhang, Q.; Zhao, C.Y.; Yang, C.S.; Sun, Q.F.; Chen, W.R. Monitoring land subsidence in the southern part of the lower Liaohe plain, China with a multi-track PS-InSAR technique. *Remote Sens. Environ.* **2017**, *188*, 73–84. [[CrossRef](#)]
32. Liu, H.X.; Yu, J.; Zhao, Z.Y.; Jezek, K. Calibrating and mosaicking surface velocity measurements from interferometric SAR data with a simultaneous least-squares adjustment approach. *Int. J. Remote Sens.* **2007**, *28*, 1217–1230. [[CrossRef](#)]
33. Liu, H.X.; Zhao, Z.Y.; Yu, J.; Jezek, K. Simultaneous least squares adjustment of multiframe velocities derived from interferometric and speckle-tracking methods. *IEEE Geosci. Remote Sens. Lett.* **2008**, *5*, 289–293.
34. Hu, J.; Li, Z.W.; Ding, X.L.; Zhu, J.J.; Sun, Q. Derivation of 3-D coseismic surface displacement fields for the 2011 Mw 9.0 Tohoku-Oki earthquake from InSAR and GPS measurements. *Geophys. J. Int.* **2013**, *192*, 573–585. [[CrossRef](#)]
35. Zhao, C.; Zhang, Q.; Yin, Y.; Lu, Z.; Yang, C.; Zhu, W.; Li, B. Pre-, co-, and post- rockslide analysis with ALOS/PALSAR imagery: A case study of the Jiweishan rockslide, China. *Nat. Hazards Earth Syst. Sci.* **2013**, *13*, 2851–2861. [[CrossRef](#)]
36. Grinsted, A.; Moore, J.C.; Jevrejeva, S. Application of the cross wavelet transform and wavelet coherence to geophysical time series, *Nonlin. Process. Geophys.* **2004**, *11*, 561–566. [[CrossRef](#)]
37. Zhang, L.; Dong, J.; Zhang, L.; Wang, Y.; Tang, W.; Liao, M. Adaptive Fusion of Multi-Source Tropospheric Delay Estimates for InSAR Deformation Measurements. *Front. Environ. Sci.* **2022**, *10*, 859363. [[CrossRef](#)]

Disclaimer/Publisher’s Note: The statements, opinions and data contained in all publications are solely those of the individual author(s) and contributor(s) and not of MDPI and/or the editor(s). MDPI and/or the editor(s) disclaim responsibility for any injury to people or property resulting from any ideas, methods, instructions or products referred to in the content.